Optical properties of hafnium-dioxide derived from reflection electron energy loss spectroscopy spectra

J.M. Gong,[a] L.H. Yang,[a] A. Sulyok,[b] Z. Baji,[b] V. Kis,[b] K. Tőkési,[c] G.J. Fang,[d] J.B. Gong,[d] X.D. Xiao[d], B. Da[e,f] and Z.J. Ding*[,a]

[a]*Hefei National Laboratory for Physical Sciences at Microscale and Department of Physics, University of Science and Technology of China, Hefei, Anhui 230026, P.R. China*

[b]*Institute for Technical Physics and Materials Science Centre for Energy Research, Budapest, Hungary*

[c]*Institute for Nuclear Research (ATOMKI), Debrecen, Hungary*

[d]*School of Physics and Technology, Wuhan University, Wuhan, Hubei 430072, P.R. China*

[e]*Research and Services Division of Materials Data and Integrated System, National Institute for Materials Science, 1-1 Namiki, Tsukuba, Ibaraki 305-0044, Japan*

[f]*Research Center for Advanced Measurement and Characterization, National Institute for Materials Science, 1-2-1 Sengen, Tsukuba, Ibaraki 305-0047, Japan*

* Corresponding author: zjding@ustc.edu.cn

Abstract

As an important gate dielectric material with high-*k* dielectric, HfO_2 is beneficial to reduce the leakage current of the complementary metal-oxide-semiconductor (CMOS) gate and improves the gate structure. In recent years, doped HfO_2 thin film materials are also believed to be a competitive candidate to replace traditional ferroelectric materials. HfO_2 also plays a key role in optical coating materials field for its high transmittance in the ultraviolet to near-infrared band, and high laser damage threshold. Therefore, it is of practical significance for the accurate knowledge of optical properties of HfO_2. Here we present high precision data of the optical constants and dielectric function of HfO_2 based on our calculated energy loss function (ELF). Our new data were derived from the analysis of the reflected electron energy loss spectra at primary electron energies of 750, 1000 and 1500 eV in the energy loss range of 0-200 eV. Sum rules are used to check the reliability of the new data. We found that the obtained ELF and thereby the optical constants and dielectric function is in the highest accuracy compared with the previously published data. Therefore, we highly recommend to replace the previous data with our present ones in a practical application.

Keywords

hafnium-dioxide, reflection electron energy loss spectroscopy, optical constants, complex dielectric function

1. Introduction

Research on the formation, properties and applications of HfO_2 material has always been active due to its hardness, high chemical stability and excellent dielectric properties. Before the 1990s, researchers generally paid attention to the crystal structure characteristics of HfO_2.[1-3] With the development of the semiconductor industry, HfO_2 has received much more attention as a representative high-*k* dielectric material which has low leakage current and good thermal stability.[4-7] In the past ten years, the ferroelectric and anti-ferroelectric properties of doped HfO_2 have gradually attracted attention for its huge potential in ferroelectric storage applications compared to traditional ferroelectric materials.[8-11] HfO_2 is also a popular candidate for planar-multilayer antenna which is able to finely adjust the distance between the director and the reflector to tune the cavity's central wavelength.[12] Due to excellent optical and thermal properties, HfO_2 has emerged as an ideal material for the improvement of absorption efficiency and thermal stability of solar energy. [13-17] In terms of electrochemistry, HfO_2 film is able to improve the performance of lithium-ion batteries.[18] HfO_2 becomes now an important material for fabricating different multilayer optical devices, such as optical coatings for astronomical CCDs and anti-reflection multilayer coatings for night vision equipment and infrared optical equipment.[19-21] Optical properties, include optical constants and dielectric function, are important indicators for measuring the performance of HfO_2 films. Jena et al. studied the aging effects on optical constants of HfO_2 thin film, which has commercial and practical significance.[22] There have been some investigations on the measurement of optical constants of HfO_2 thin films using the spectroscopic ellipsometry method or the transmission spectroscopy method.[20,22-27] The maximum photon energy adopt in these measurements are only up to several eVs and the measurement accuracy is limited by the optical resolution. Ikarashi et al. used the electron energy loss spectrum in low energy-loss region (0-100 eV) combined with theoretical calculations to obtain the relative value of the energy loss function (ELF) of polycrystalline HfO_2.[29] Later Jin et al.[30] conducted a quantitative analysis of ELF of ultra-thin HfO_2 on Si(100) by using Tougaard-Yubero QUEELS-ε(k,ω)-REELS software,[31] where the crystalline state was not explicitly stated but most likely to be the amorphous according to their sample preparation method.[32] Cheynet et al. employed the valence electron energy loss spectroscopy to investigate the crystal structure and the band gap of HfO_2 thin films.[33] It was found that the peak position and shape are affected by the crystal structure and thereby the optical properties. In addition to the experimental methods, some theoretical calculations are also applied to obtain the dielectric and optical properties, for example, Sklénard et al. reported the electronic structure and optical properties of different crystalline HfO_2 by the first principles calculations.[34]

In this work we have combined the reflection electron energy loss spectroscopy (REELS) spectra measurement and the unique reverse Monte Carlo (RMC) method developed based on the electron-surface interaction model[35-44] to extract the high-precision ELF of nanocrystalline HfO_2. Based on this high-precision ELF, we present the optical constants and dielectric function of the HfO_2 film.

2. Experimental

The HfO_2 film was grown by atomic layer deposition (ALD) with a Picosun R-200 ALD equipment on Si wafer in thickness of 90 nm. Prior to deposition the wafer was cleaned with HNO_3 and deionized water. The used precursors were 98% purity tetrakis (dimethylamino) hafnium (TDMAH) purchased from Strem Chemicals, Inc. and 18 MΩ purity deionized water as oxidant. The TDMAH was heated to 105 °C to achieve the vapor pressure sufficient for deposition. The deposition temperature was 120 °C which is within the ALD window of HfO_2 growth, and yields smooth and uniform films. The pulse lengths were set as 0.2 s pulses and 6 s purging after each pulse, which is the double of that generally used for planar surfaces. But as HfO_2 deposition tends to include a parasitic chemical vapor deposition-like growth, the longer pulses ensured a clean ALD growth.

Before the REELS measurements our sample was analyzed by a transmission electron microscopy (TEM) using a FEI Titan-Themis transmission electron microscope with a Cs corrected objective lens (point resolution is around 0.09 nm in high resolution mode) operated at 200 kV. The TEM sample was prepared using focused ion beam milling with an FEI Scios 2 DualBeam System. For rough milling 30 keV and later 16 keV Ga beam was used, and by reaching ca. 100 nm lamella thickness the ion energy was reduced to 5 keV. Final polishing was done by using 2 keV beam. Figure 1(a) shows by TEM image that the HfO_2 film is polycrystalline with the nanoscale grain size. The size of the individual nanocrystals is typically in the range between 3 and 6 nm; however, in minor amount both larger and smaller grains can be found. The crystal structure of the film was further checked by high resolution transmission electron microscopy (HRTEM) image in Figure 1(b). The HRTEM image revealing the atomic planes of crystals shows the different orientation of grains. According to the Fourier transform made from about 50x50 nm area we concluded that the HfO_2 layer is nanocrystalline. The even distribution of intensity along the diffraction rings indicates that the nanocrystals are in random orientation, no preferred growth direction can be observed. The interplanar spacings determined from the Fourier transform are in good agreement with those of orthorombic HfO_2.[45]

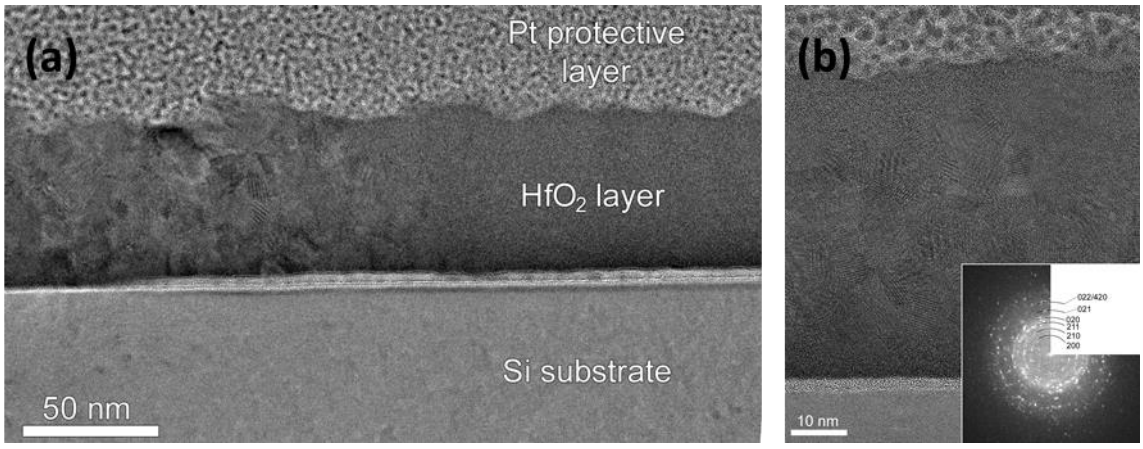

Figure 1 (a) TEM image of HfO_2 layer in cross section. (b) HRTEM image of the HfO_2 layer. Fourier transform of the layer is shown in the insert.

REELS spectra were detected in reflection mode at primary energies of 750, 1000 and 1500 eV in UHV of $7x10^{-10}$ mbar. The current of the electron beam varies with the primary energy. To avoid any influence of the detection system on the

measured REELS spectra the beam current at any primary energy was adjusted so that the highest intensity (top of the elastic peak) was around 4×10^5 counts/s, which is well below the saturation level of the detection system. Electron beam excitation was provided by an electron gun at 54° angle of incidence with respect the surface normal (Figure 2). REELS spectra were detected by a special retarding field cylindrical mirror analyzer DESA 150 (Staib Instruments) with a constant energy resolution of 3 eV. The collection angle (take-off angle) of the analyzer was $22^o \pm 5^o$, with respect the surface normal. The first 200 eV wide section of spectrum including the elastic peak and the energy loss part was detected with energy step of 0.1 eV. Apart from the elastic peak the intensity of spectra was low, therefore, several measured spectra were averaged to improve the statistics.

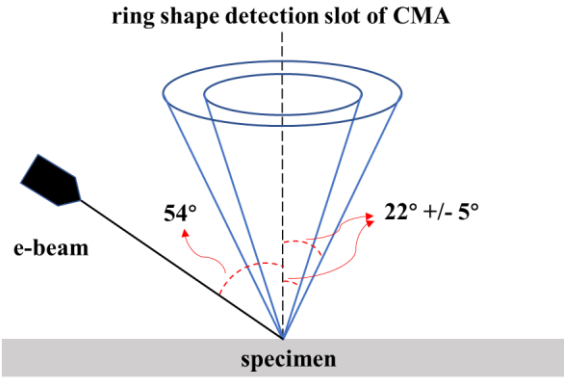

Figure 2. Schematic diagram for the geometry of REELS experiments.

3. Theoretical

The ELF and, hence, the optical constants and dielectric function were obtained based on a RMC simulation of REELS spectrum, which uses the dielectric response theory combined with the simulated annealing algorithm. This RMC simulation improves the calculation efficiency while maintaining high precision.[38-45] In Monte Carol simulation the Mott's cross-section is used to describe elastic scattering of electrons and we consider both surface excitation and bulk excitation when dealing with the inelastic interaction of electrons with a solid.[46] The Mott's differential cross-section is expressed as,

$$\frac{d\sigma_e}{d\Omega} = \left|f(\theta)\right|^2 + \left|g(\theta)\right|^2, \tag{1}$$

where σ_e represents elastic scattering cross-section, θ is scattering angle, with scattering amplitudes,

$$f(\theta) = \frac{1}{2iK}\sum_l \left\{(l+1)\left[\exp\left(2i\delta_l^+\right)-1\right] + l\left[\exp\left(2i\delta_l^-\right)-1\right]\right\} P_l(\cos\theta); \tag{2}$$

$$g(\theta) = \frac{1}{2iK}\sum_l \left[\exp\left(2i\delta_l^-\right) - \exp\left(2i\delta_l^+\right)\right] P_l^1(\cos\theta), \tag{3}$$

where $P_l(\cos\theta)$ and $P_l^1(\cos\theta)$ are the Legendre and the first-order associated Legendre functions, respectively; δ_l^+ and δ_l^- are spin-up and spin-down phase shifts of the *l*th partial wave, respectively.

A semi-classical model is applied to describe electron inelastic scattering near the surface region, where the depth dependent inelastic scattering cross-section $\sigma(z)$ is given by,

$$\begin{aligned}\sigma(z)=&\frac{2}{\pi v^2}\int_{q_-}^{q_+}dq\frac{1}{q}\mathrm{Im}\left[\frac{-1}{\varepsilon(\vec{q},\omega)}\right]\Theta(-z)+\frac{4\cos\alpha}{\pi^3}\int_{q_-}^{q_+}dq\int_0^{\frac{\pi}{2}}d\theta\int_0^{2\pi}d\phi\frac{q\sin^2\theta\cos(q_\perp z)\exp(q_\parallel z)}{\tilde{\omega}^2+q_\parallel^{\,2}v_\perp^{\,2}}\\&\times\left\{\mathrm{Im}\left[\frac{-1}{\varepsilon(\vec{q}_\parallel,\omega)+1}\right]-\frac{1}{2}\mathrm{Im}\left[\frac{-1}{\varepsilon(\vec{q}_\parallel,\omega)}\right]\right\}\Theta(-z)\\&+\frac{4\cos\alpha}{\pi^3}\int_{q_-}^{q_+}dq\int_0^{\frac{\pi}{2}}d\theta\int_0^{2\pi}d\phi\frac{q\sin^2\theta\exp(-q_\parallel z)}{\tilde{\omega}^2+q_\parallel^{\,2}v_\perp^{\,2}}\mathrm{Im}\left[\frac{-1}{\varepsilon(\vec{q}_\parallel,\omega)+1}\right]\left[2\cos\left(\frac{\tilde{\omega}z}{v\cos\alpha}\right)-\exp(-q_\parallel z)\right]\Theta(z),\quad v_\perp>0\end{aligned}\tag{4}$$

and

$$\begin{aligned}\sigma(z)=&\frac{2}{\pi v^2}\int_{q_-}^{q_+}dq\frac{1}{q}\mathrm{Im}\left[\frac{-1}{\varepsilon(\vec{q},\omega)}\right]\Theta(-z)+\frac{4\cos\alpha}{\pi^3}\int_{q_-}^{q_+}dq\int_0^{\frac{\pi}{2}}d\theta\int_0^{2\pi}d\phi\frac{q\sin^2\theta\cos(-q_\perp z)\exp(-q_\parallel z)}{\tilde{\omega}^2+q_\parallel^{\,2}v_\perp^{\,2}}\\&\times\mathrm{Im}\left[\frac{-1}{\varepsilon(\vec{q}_\parallel,\omega)+1}\right]\Theta(z)+\frac{4\cos\alpha}{\pi^3}\int_{q_-}^{q_+}dq\int_0^{\frac{\pi}{2}}d\theta\int_0^{2\pi}d\phi\\&\times\frac{q\sin^2\theta\exp(q_\parallel z)}{\tilde{\omega}^2+q_\parallel^{\,2}v_\perp^{\,2}}\left\{\mathrm{Im}\left[\frac{-1}{\varepsilon(\vec{q}_\parallel,\omega)+1}\right]-\frac{1}{2}\mathrm{Im}\left[\frac{-1}{\varepsilon(\vec{q}_\parallel,\omega)}\right]\right\}\left[2\cos\left(\frac{\tilde{\omega}z}{v\cos\alpha}\right)-\exp(q_\parallel z)\right]\Theta(-z),\quad v_\perp<0\end{aligned}\tag{5}$$

where $\tilde{\omega}=\omega-qv\sin\theta\cos\phi\sin\alpha$, $q_\parallel=q\sin\theta$ and $E=v^2/2$. The upper and lower limits of the integrals come from the energy and momentum conservation laws: $q_\pm=\sqrt{2E}\pm\sqrt{2(E-\omega)}$. Figure 3 shows the geometry for the electron movement in relative to the material.

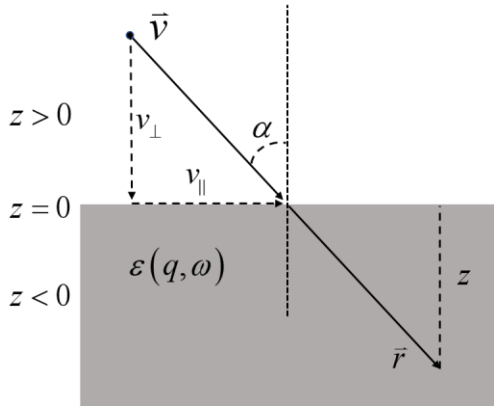

Figure 3. The geometry of the interaction between an electron and material. The depth position of the electron is z ($z=|\vec{r}|\cos\alpha$) and the velocity is $\vec{v}$ ($v_\parallel=v\sin\alpha$, $v_\perp=v\cos\alpha$).

The ELF is expressed here as the superposition of dozens of Drude-Lidhard dielectric function oscillators,

$$\mathrm{Im}\left[\frac{-1}{\varepsilon(\omega)}\right]=\sum_{i=1}^{N}A_i\,\mathrm{Im}\left[\frac{-1}{\varepsilon_D(\omega;\omega_{pi},\gamma_i)}\right],\tag{6}$$

where A_i, ω_{pi} and γ_i are oscillator coefficients representing for the strength, energy and width of the *i*th oscillator, respectively. Ritchie and Howie's theoretical method is adopted to extrapolate the ELF at the optical limit to the general case of non-zero momentum.[47-48] During the simulations we used $N = 56$ oscillators.

4. Results and Discussion

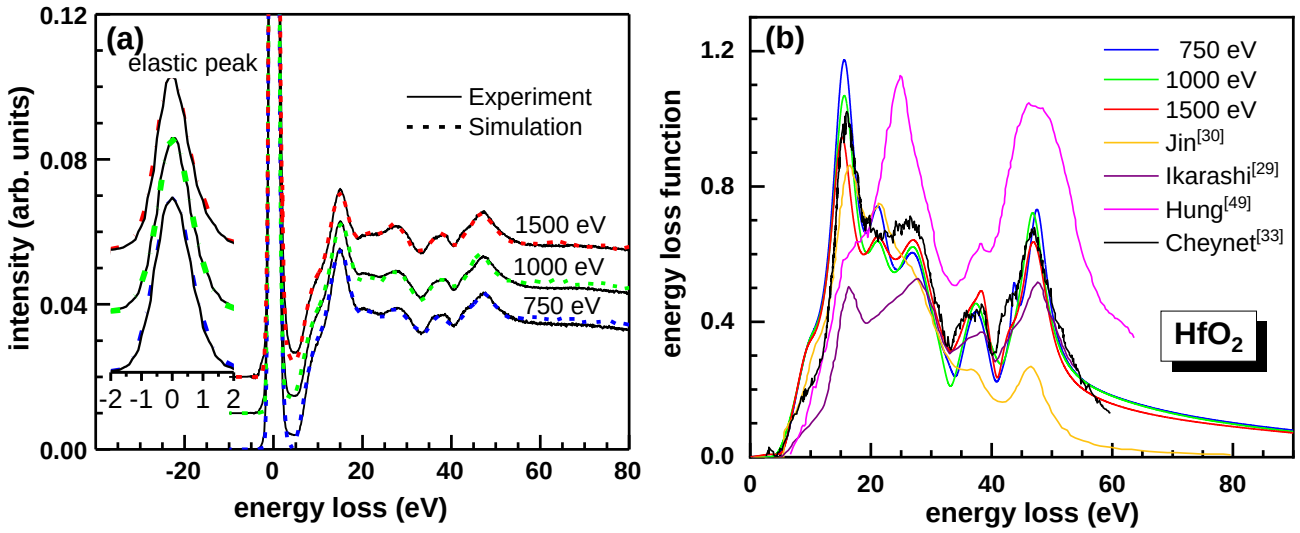

Figure 4. (a) The final simulated REELS spectra (dashed line) in comparison with experimental spectra (solid line) at primary electron energies of 750, 1000 and 1500 eV; (b) The ELF of HfO_2 extracted from the REELS spectra in comparison with the previous results (ELFs or the direct EELS spectra).[29-30,33,49]

The comparison between the RMC simulation results and the experimental REELS spectra is shown in Figure 4(a). The REELS spectra are normalized with the elastic peak height. In the experimental REELS spectra several characteristic energy loss peaks at ~10, 15, 21, 27.5, 37 and 46.5 eV can be identified, where the peak positions are close to the previous data but our peak intensities are much pronounced.[30] The peak at ~9 eV is due to single particle transition (O 2p → Hf 5d), as well as 21 eV (O 2s → Hf 5d) and 37 eV (Hf 5p → 5d). The 15 eV peak is attributed to a real bulk plasmon, while the peaks at ~27 and 46.5 eV are uncertified collective excitations.[28,34] The simulated and the experimental spectra are in better agreement at higher primary beam energies due to partly of the fast electron approximation[48] employed in the theoretical model. The ELFs extracted from the corresponding REELS spectra are shown in Figure 4(b) in comparison with the previous experimental ELFs or the direct measured EELS spectra.[29-30,33,49]

One should note that Ikarashi et al. presented only the relative intensity of ELF. In addition, the EELS spectrum contains contributions from surface excitation and multiple scattering components and, thus, does not exactly correspond to ELF so that their peak positions may differ. Our peak positions of ELF are compared with the previous peak positions of ELF or EELS spectra in TABLE I. Since the spectra of the single scattering distribution (SSD) is theoretically proportional to ELF,[56] we can directly compare their peak positions. It can be seen that the peak positions of our ELF agree well with peak positions of the spectra of the SSD in the Ref [33][b]. While in "Ref. [33][a]" two peaks are missing in "Ref. [49][c]". "Ref. [30][d]" and "Ref. [29][e]" also lack one peak each. The reasons for the missing of peaks maybe due

to the difference in crystalline structure, the limitation by detector energy resolution and/or unresolved feature in the direct EELS spectra.

TABLE I. Comparison of peak positions (eV) of ELF of HfO_2 with literatures.

present	nanocrystalline (orthorhombic)	9.5	15.5	21.2	27	37.2	42.8	46.4
Ref. [33][a]	bulk (unknown phase)	8.2	15	-	27.3	36.8	42.5	46.4
Ref. [33][b]	crystalline+nanocrystalline (monoclinic+orthorhombic)	9.2	15.7	-	26.8	37.1	42.5	47.0
Ref. [49][c]	polycrystalline(monoclinic)	12	15.5	-	24.9	38.3	-	47.3
Ref. [30][d]	amorphous	10.5	16.5	21.5	26.6	36.9	-	46.6
Ref. [29][e]	polycrystalline (unknown phase)	9.0	16.3	-	27.7	38.8	43.4	47.6

[a]*figure 4a in Ref. [33], VEELS spectra of "HfO_2-reference".*
[b]*figure 5a in Ref. [33], SSD spectra of HfO_2.*
[c]*figure 2 in Ref. [49], HRTEM-VEELS spectra of HfO_2.*
[d]*figure 3 in Ref. [30], ELF of HfO_2*
[e]*figure 1 in Ref. [29], ELF of HfO_2*

From the ELF one can derive the corresponding complex dielectric function and optical constants according to Kramers-Kronig relation. The complex dielectric function is as follows:

$$\varepsilon_1 = \frac{-\mathrm{Re}\left[-1/\varepsilon(\omega)\right]}{\mathrm{Im}\left[-1/\varepsilon(\omega)\right]^2 + \mathrm{Re}\left[-1/\varepsilon(\omega)\right]^2}; \tag{7}$$

$$\varepsilon_2 = \frac{\mathrm{Im}\left[-1/\varepsilon(\omega)\right]}{\mathrm{Im}\left[-1/\varepsilon(\omega)\right]^2 + \mathrm{Re}\left[-1/\varepsilon(\omega)\right]^2}, \tag{8}$$

and the refractive index n and extinction coefficient k are expressed as:

$$n = \sqrt{\frac{\varepsilon_1 + \sqrt{\varepsilon_1^2 + \varepsilon_2^2}}{2}}; \tag{9}$$

$$k = \sqrt{\frac{-\varepsilon_1 + \sqrt{\varepsilon_1^2 + \varepsilon_2^2}}{2}}. \tag{10}$$

Several sum rules were used to check the validity of our obtained data, including a) the inertial sum rule, Eq. (11); b) the dc-conductivity sum rule, Eq. (12); c) the perfect-screening sum rule (*ps*-sum rule), Eq. (13) and d) the oscillator-strength sum rule (*f*-sum rule), Eqs. (14)-(16),[50-52]

$$R_n(\omega) = \int_0^{\omega} \left[n(\omega') - 1\right] d\omega'; \tag{11}$$

$$R_{\varepsilon_1}(\omega) = \int_0^{\omega} \left[\varepsilon_1(\omega') - 1\right] d\omega'; \tag{12}$$

$$P_{eff}\big|_{ELF} = \frac{2}{\pi}\int_0^{\infty} \frac{1}{\omega}\,\mathrm{Im}\left[-1/\varepsilon(\omega)\right] d\omega + \mathrm{Re}\left[-1/\varepsilon(0)\right]; \tag{13}$$

$$\mathrm{Z}_{eff}\big|_{ELF} = \frac{2}{\pi\Omega_p^2}\int_0^{\infty} \omega\,\mathrm{Im}\left[-1/\varepsilon(\omega)\right] d\omega; \tag{14}$$

$$\mathrm{Z}_{eff}\big|_{\varepsilon_2} = \frac{2}{\pi\Omega_p^2}\int_0^{\infty} \omega\varepsilon_2(\omega)\, d\omega; \tag{15}$$

$$\mathrm{Z}_{eff}\big|_{k} = \frac{4}{\pi\Omega_p^2}\int_0^{\infty} \omega k(\omega)\, d\omega, \tag{16}$$

where $n(\omega)$ is refractive index, $k(\omega)$ the extinction coefficient, $\varepsilon_1(\omega)$ and $\varepsilon_2(\omega)$ are the real and imaginary parts of dielectric function, $\hbar\Omega_p = \sqrt{4\pi n_a/m}$, and n_a is the atomic density of the sample. In Eqs. (11)-(12), the theoretical nominal limit value is 0 when $\omega \to \infty$, while it is 1 for the *ps*-sum rule in Eq. (13). For *f*-sum rule in Eqs. (14)-(16) the limit value equals to the sum of atomic numbers of elements. Our ELF is obtained in the energy loss (or photon energy) range of 0-200 eV. For higher energy loss region used in the sum rules, we adopt data in Henke database for 200 eV-30 keV[53] and the calculated data by atomic scattering factors for 30 keV-10 MeV.[54] The relative error is used to describe the difference between the obtained sum rules and the theoretical value. Since the theoretical limit value is 0 for Eqs. (11)-(12), the traditional definition of relative error cannot be used. Here, we adopt a new definition[50] of relative errors as:

$$\xi_n = \frac{\int_0^\infty [n(\omega)-1]d\omega}{\int_0^\infty |n(\omega)-1|d\omega}; \tag{17}$$

$$\xi_{\varepsilon_1} = \frac{\int_0^\infty [\varepsilon_1(\omega)-1]d\omega}{\int_0^\infty |\varepsilon_1(\omega)-1|d\omega}, \tag{18}$$

for the inertial sum rule and dc-conductivity sum rule, respectively. A root-mean-square deviation (RMS) of *f*-sum rules,

$$\mathrm{RMS} = 100 \times \sqrt{\frac{1}{3}\sum_{i=1}^{3}\left(\frac{Z_{eff,i} - \bar{Z}_{eff}}{\bar{Z}_{eff}}\right)^2} \quad (\%) \tag{19}$$

is used to describe the difference between the *f*-sum rules in Eqs. (14)-(16), where $Z_{eff,i}$ represents $Z_{eff}|_{ELF}$, $Z_{eff}|_{\varepsilon_2}$ and $Z_{eff}|_k$, respectively and $\bar{Z}_{eff}$ is the mean value of the three *f*-sum rule results.

TABLE II. List of inertial and dc-conductivity sum rule checks of HfO_2 with their relative errors.

E[a] (eV)	$R_n(\infty)$	ξ_n	$R_{\varepsilon_1}(\infty)$	ξ_{ε_1}	$P_{eff}\|_{ELF}$	relative error for $P_{eff}\|_{ELF}$ (%)
750	-4.203	-0.165	-0.423	-0.136	1.0389	3.89
1000	-1.666	-0.072	-0.168	-0.060	1.0128	1.28
1500	-0.325	-0.015	-0.032	-0.012	0.9996	-0.04

[a]E is the primary energy of electron beam.

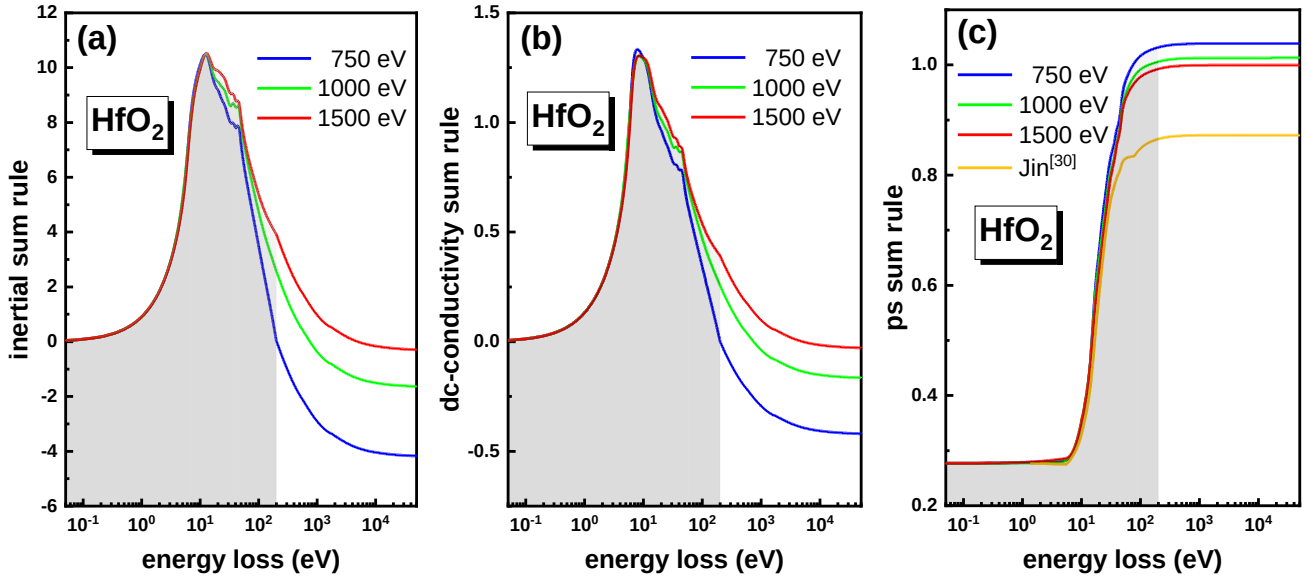

Figure 5. The results of three different sum rules: (a) inertial sum rule using Eq. (11); (b) dc-conductivity sum rule using Eq. (12); (c) *ps*-sum rule using Eq. (13). The shaded area shows the contribution from the present data.

The results of inertial, dc-conductivity and *ps*-sum rules for 750, 1000 and 1500 eV are shown in Figure 5. Since HfO_2 is a semiconductor, $\mathrm{Re}\left[-1/\varepsilon(0)\right]$ is approximately $1/n^2(0)$ in *ps*-sum rule, where $n(0)=1.91$ is the refractive index of HfO_2 in the optical limit based on the Sopra Material Database.[57] The exact numerical results are listed in Table II. From the table we can see that the values of the inertial and dc-conductivity sum rules for the primary electron energy of 1500 eV are quite close to 0, so it certificate the high accuracy of the dielectric function and optical constants (see ξ_n = -0.015 and ξ_{ε_1} = -0.012 in Table II.). Furthermore, for all three energies the obtained results of *ps*-sum rule are close to 1, which is the nominal theoretical value. This fact also confirm the accuracy of our results.

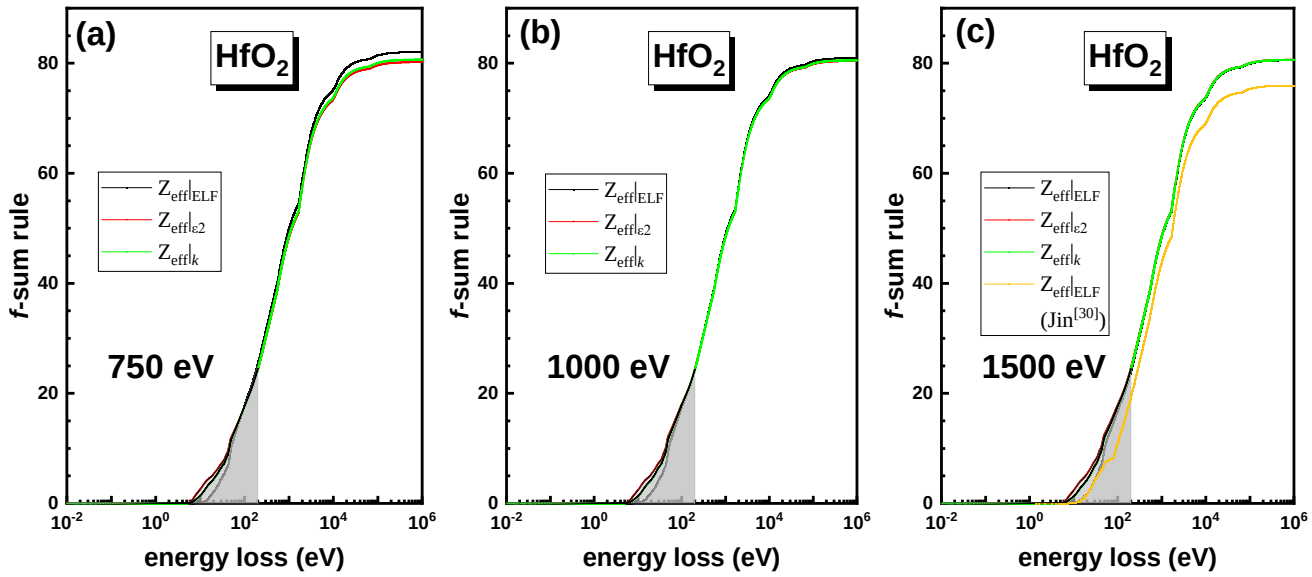

Figure 6. Results of *f*-sum rules using Eqs. (14)-(16) for primary electron energy: (a) 750 eV; (b) 1000 eV; (c) 1500 eV. The shaded area shows the contribution from the present data.

TABLE III. The list of the three *f*-sum rules, their average values, relative errors and RMS.

E[a] (eV)	$Z_{eff}\|_{ELF}$	$Z_{eff}\|_{\varepsilon_2}$	$Z_{eff}\|_{k}$	$\bar{Z}_{eff}$ [b]	relative error for $\bar{Z}_{eff}$ (%)	RMS (%)
750	82.079	80.220	80.678	80.992	-7.964	0.976
1000	81.005	80.422	80.567	80.665	-8.335	0.307
1500	80.580	80.641	80.625	80.615	-8.392	0.032

[a] E is the primary energy of electron beam.

[b] $\bar{Z}_{eff}$ is the average value of the *f*-sum rules for ELF, ε_2 and k.

The nominal value for each of the *f*-sum rules should be the sum of the atomic numbers of the constituent elements for a compound, i.e., 88 for HfO_2. We note that the major contribution to the calculations of *f*-sum rule originates from the energy loss greater than 200 eV, while our data in the range of 0-200 eV makes only a small partial contribution as seen from Figure 6. Therefore, the data in Henke's database[53] and calculated by atomic scattering factors[54] more affect the accuracy of the sum rules. When the phonon energy is more than a few keV, the refractive index $n(\varepsilon)$ is very close to unit and we can write $\mathrm{Im}(-1/\varepsilon) \propto \varepsilon_2 \propto 2k$. Therefore, the integrals of the three different *f*-sum rules in this energy range are equivalent. This means that the RMS which represents the difference between the three *f*-sum rules mainly comes from the accuracy of ELF, ε_2 and k in the low energy loss region. From Table III one can see that RMS is very small. This result further demonstrates that the ELF, optical constants and dielectric function extracted by the REELS spectra are reliable. The sum rules obtained according to previous published data[30] are also shown in Figure 5(c) & Figure 6(c), illustrating that our results have the higher accuracy.

Finally, we have determined the optical constants and dielectric function of HfO_2 based on the REELS spectra. Figure 7(a) and Figure 7(b) show the reactive index n and extinction coefficient k, real part (ε_1) and imaginary part (ε_2) of dielectric function in a wide photon energy range of 0-200 eV, respectively. The real part and imaginary part of dielectric function with energy loss of 0-30 eV compared with previous first principles calculation results are presented in Figure 7(c) and Figure 7(d), respectively. We choose the band gap to be 5 eV in our simulation. The variation on the dielectric function when the band gap is varied between 4-6 eV is indicated by the shaded area in the Figure 7(c) and Figure 7(d). From the result we can see our data is similar to the cubic-HfO_2 result of Li et al.[58] Sklénard et al.[34] have calculated the imaginary part (ε_2) of dielectric function for three phases and all (100)-, (010)-, (001)-polarization directions, and the result presented in Figure 7(d) is the averaged value of three polarization directions for each crystalline phase.

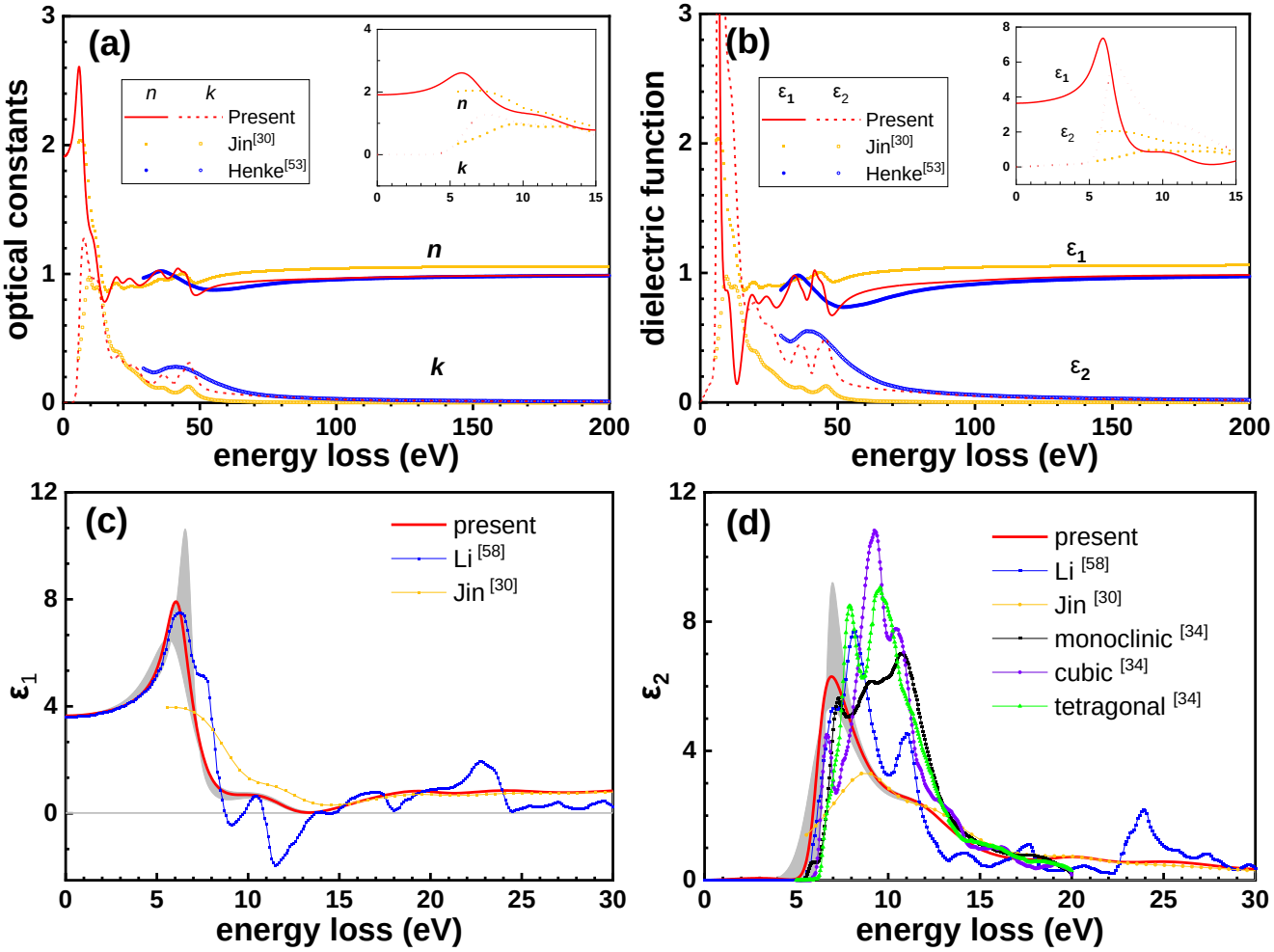

Figure 7. Comparison of optical constants and dielectric function obtained from REELS with the data of literature.[30,53,58,34] (a) The refractive index *n* and extinction coefficient *k* as a function of energy loss; (b) The real part (ε_1) and imaginary part (ε_2) of dielectric function as functions of energy loss; (c) The real part (ε_1) in energy loss range of 0-30 eV; (d) The imaginary part (ε_2) in energy loss range of 0-30 eV, where the curves for monoclinic, cubic and tetragonal phases are from the first principles calculations.

5. Conclusion

The combined experimental and theoretical studies of the optical properties of the HfO_2 sample based on the ELF were presented. REELS spectra were measured on clean HfO_2 sample at 750, 1000 and 1500 eV primary energies. RMC method was applied using our high accuracy REELS spectra to extract the ELFs in the 0-200 eV range. We found that the simulated and the measured spectra are in excellent agreement with each other. From the ELF the corresponding complex dielectric function and the optical constants were calculated. The accuracy of our data was justified by using various sum rules. Based on the sum-rules results the obtained ELF and the derived optical constants and dielectric function show high accuracy. We found that our data are much closer to the nominal theoretical values of sum rules than any others. Due to the accuracy of the new data the use of our data in materials science is highly recommended for further applications.

Author contributions

J.M. Gong: Validation, Formal analysis, Writing – original draft, Visualization. **L.H. Yang:** Methodology, Formal analysis. **A. Sulyok:** Investigation, Resources. **Z. Baji:** Investigation, Resources. **V. Kis:** Investigation, Resources. **K. Tőkési:** Conceptualization, Writing – original draft, Writing – review & editing. **G.J. Fang**: Investigation, Resources. **J.B. Gong:** Investigation, Resources. **X.D. Xiao:** Investigation, Resources. **B. Da:** Conceptualization, Methodology. **Z.J. Ding:** Conceptualization, Methodology, Software, Writing – review & editing, Supervision, Project administration, Funding acquisition.

Conflict of Interest

There are no conflicts to declare.

Acknowledgements

The work was supported by the National Key Research and Development Project (2019YFF0216404) and Education Ministry through "111 Project 2.0" (BP0719016), and by European Cost Actions CA18212 (MDgas). We thank also Dr. H.M. Li and the supercomputing center of USTC for the support of parallel computing.

References

[1] J. Adam and M. D. Rogers, Acta Crystallogr. **1959**, 12, 951.

[2] P. Kofstad and D. J. Ruzicka, J. Electrochem. Soc. **1963**, 110, 181.

[3] R. E. Hann, P. R. Suitch, and J. L. Pentecost, J. Am. Ceram. Soc. **1985**, 68, C285.

[4] C. T. Kuo, R. Kwor, and K. M. Jones, Thin Solid Films **1992**, 213, 257.

[5] K. Kukli, J. Ihanus, M. Ritala, M. Leskela, Appl. Phys. Lett. **1996**, 68, 3737.

[6] C. T. Hsu, Y. K. Su, and M. Yokoyama, Jpn. J. Appl. **1992**, 31, 2501.

[7] L. Kang, B. H. Lee, W. J. Qi, Y. Jeon, R. Nieh, S. Gopalan, K. Onishi, J. C. Lee, IEEE Elect. Dev. Lett. **2000**, 21, 181.

[8] Z. Fan, J. S. Chen, J. Wang, J. Adv. Dielectr. **2016**, 6, 1630003.

[9] L. Xu, T. Nishimura, S. Shibayama, T. Yajima, S. Migita, A. Toriumi, Appl. Phys. Express **2016**, 9, 091501.

[10] J. Müller, E. Yurchuk, T. Schlösser, J. Paul, R. Hoffmann, S. Müller, D. Martin, S. Slesazeck, P. Polakowski, J. Sundqvist, M. Czernohorsky, K. Seidel, P. Kücher, R. Boschke, M. Trentzsch, K. Gebauer, U. Schröder, T. Mikolajick, in: *2012 Symposium on VLSI Technology (VLSIT)*, Honolulu, HI, USA, 12 June-14 June **2012**, pp. 25-26.

[11] S. Clima, D. J. Wouters, C. Adelmann, T. Schenk, U. Schroeder, M. Jurczak, G. Pourtois, Appl. Phys. Lett. **2014**, 104, 092906.

[12] H. Huang, S. Manna, C. Schimpf, M. Reindl, X. Yuan, Y. Zhang, S. F. C. da Silva, A. Rastelli, Adv. Opt. Mater. **2021**, 9, 2001490.

[13] D. Shin, G. Kang, P. Gupta, S. Behera, H. Lee, A. M. Urbas, W. Park, K. Kim, Adv. Opt. Mater. **2018**, 6, 1800317.

[14] Y. Wang, L. Zhou, Y. Zhang, J. Yu, B. Huang, Y. Wang, Y. Lai, S. Zhu, J. Zhu, Adv. Opt. Mater. **2018**, 6, 1800813.

[15] M. Chirumamilla, A. Chirumamilla, Y. Yang, A. S. Roberts, P. K. Kristensen, K. Chaudhuri, A. Boltasseva, D. S. Sutherland, S. I. Bozhevolnyi, K. Pedersen, Adv. Opt. Mater. **2017**, 5, 1700552.

[16] S. Wu, Y. Ye, Z. Jiang, T. Yang, L. Chen, Adv. Opt. Mater. **2019**, 7, 1901162.

[17] D. W. Lee, M. F. Bhopal, S. H. Lee, A. R. Lee, H. J. Kim, M. A. Rehman, Y. Seo, K. Lim, W. Shin, S. H. Lee, Energy Sci. Eng. **2018**, 6, 706.

[18] N. Yesibolati, M. Shahid, W. Chen, M. N. Hedhili, M. C. Reuter, F. M. Ross, H. N. Alshareef, Small, **2014**, 10, 2849.

[19] M. Lesser, Opt. Eng. **1987**, 26, 911.

[20] M. Fadel, O. A. Azim, O. A. Omer, R. R. Basily, Appl. Phys. A **1998**, 66, 335.

[21] F. L. Martinez, M. Toledano-Luque, J. J. Gandia, J. Carabe, W. Bohne, J. Rohrich, E. Strub, I. Martil, J. Phys. D **2007**, 40, 5256.

[22] S. Jena, R. B. Tokas, S. Thakur, D. V. Udupa, Optik **2019**, 185, 71.

[23] J. M. Khoshman, M. E. Kordesch, Surf. Coat. Technol. **2006**, 201, 3530.

[24] J. Sancho-Parramon, M. Modreanu, S. Bosch, M. Stchakovsky, Thin Solid Films **2008**, 516, 7990.

[25] D. Franta, I. Ohlidal, D. Necas, F. Vizda, O. Caha, M. Hason, P. Pokorny, Thin Solid Films **2011**, 519, 6085.

[26] Y. S. Lin, R. Puthenkovilakam, J. P. Chang, Appl. Phys. Lett. **2002**, 81, 2041.

[27] N. M. Kamble, R. B. Tokas, A. Biswas, S. Thakur, D. Bhattacharyya, N. K. Sahoo, Vacuum **2011**, 86, 422.

[28] C. Guedj, L. Hung, A. Zobelli, P. Blaise, F. Sottile, V. Olevano, Appl. Phys. Lett. **2014**, 105, 222904.

[29] N. Ikarashi, K. Manabe, J. Appl. Phys. **94**, 480 (2003).

[30] H. Jin, S. K. Oh, H. J. Kang, S. Tougaard, J. Appl. Phys. **2006**, 100, 083713.

[31] S. Tougaard, F. Yubero, Surf. Interface Anal. **2004**, 36, 824.

[32] D. H. Triyoso, R. I. Hegde, B. E. White Jr, P. J. Tobin, J. Appl. Phys. **2005**, 97, 124107.

[33] M. C. Cheynet, S. Pokrant, F. D. Tichelaar, J.-L. Rouvière, J. Appl. Phys. **2007**, 101, 054101.

[34] B. Sklénard, A. Dragoni, F. Triozon, V. Olevano, Appl. Phys. Lett. **2018**, 113, 172903.

[35] R. Shimizu, Z. J. Ding, Rep. Prog. Phys. **1992**, 55, 487.

[36] Z. J. Ding, R. Shimizu, Scanning **1996**, 18, 92.

[37] Z. J. Ding, K. Salma, H. M. Li, Z. M. Zhang, K. Tokesi, D. Varga, J. Toth, K. Goto, R. Shimizu, Surf. Interface Anal. **2006**, 38, 657.

[38] B. Da, Y. Sun, S. F. Mao, Z. M. Zhang, H. Jin, H. Yoshikawa, S. Tanuma, Z. J. Ding, J. Appl. Phys. **2013**, 113, 214303.

[39] H. Xu, B. Da, J. Toth, K. Tokesi, Z. J. Ding, Phys. Rev. B **2017**, 95, 195417.

[40] H. Xu, L. H. Yang, B. Da, J. Tóth, K. Tőkési, Z. J. Ding, Nucl. Instrum. Methods Phys. Res. B **2017**, 406, 475.

[41] H. Xu, L. H. Yang, J. Tóth, K. Tőkési, B. Da, Z. J. Ding, J. Appl. Phys. **2018**, 123, 043306.

[42] L. H. Yang, M. Menyhard, A. Sulyok, K. Tőkési, Z. J. Ding, Appl. Surf. Sci. **2018**, 456, 999.

[43] L. H. Yang, J. Tóth, K. Tőkési, B. Da, Z. J. Ding, Eur. Phys. J. D **2019**, 73, 21.

[44] L. H. Yang, K. Tokesi, J. Toth, B. Da, H. M. Li, Z. J. Ding, Phys. Rev. B **2019**, 100, 245209.

[45] I. Levin, NIST Inorganic Crystal Structure Database (ICSD), National Institute of Standards and Technology (**2018**), https://data.nist.gov/od/id/mds2-2147.

[46] Y. C. Li, Y. H. Tu, C. M. Kwei, C. J. Tung, Surf. Sci. **2005**, 589, 67.

[47] R. H. Ritchie, A. Howie, Philos. Mag. **1977**, 36, 463.

[48] D. R. Penn, Phys. Rev. B **1987**, 35, 482.

[49] L. Hung, C. Guedj, N. Bernier, P. Blaise, V. Olevano, F. Sottile, Phys. Rev. B **2016**, 93, 165105.

[50] M. Altarelli, D. Y. Smith, Phys. Rev. B **1974**, 9, 1290.

[51] E. Shiles, T. Sasaki, M. Inokuti, D. Y. Smith, Phys. Rev. B **1980**, 22, 1612.

[52] E. D. Palik eds., *Handbook of Optical Constants of Solids* (Academic Press, **1998**).

[53] B. L. Henke, E. M. Gullikson, J. C. Davis, At. Data Nucl. Data Tables **1993**, 54, 2.

[54] D. E. Cullen, J. H. Hubbell, L. Kissel, EPDL97, the Evaluated Photon Data Library, UCRL-50400 **1997**, 6, 1-28.

[55] C. R. Garibotti, P. A. Massaro, J. Phys. B **1971**, 4, 79.

[56] T. Kiguchi, N. Wakiya, K. Shinozaki, T. J. Konno, Mater. Sci. Eng. B **2009**, 161, 160.

[57] SOPRA, Refractive Index Libirary, http://www.sspectra.com/contents.html

[58] J. Li, S. Meng, L. Li, H. Lu, T. Tohyama, Comput. Mater. Sci. **2014**, 81, 397.